# Design of artificial molecular motor inheriting directionality and scalability.

**Kenta I. Ito**[1], **Yusuke Sato**[2], **and Shoichi Toyabe**[1,*]

[1]Department of Applied Physics, Graduate School of Engineering, Tohoku University, Sendai 980-8579, Japan
[2]Department of Intelligent and Control Systems, Kyushu Institute of Technology, Fukuoka 820-8502, Japan
[*]toyabe@tohoku.ac.jp

## ABSTRACT

The realization of artificial molecular motors with autonomous functionality and high performance is one of the major challenges in biophysics. Such motors provide not only new dimensions in biotechnologies but also a novel approach for the bottom-up elucidation of biological molecular motors. For practical applications, directionality and scalability are critical factors. However, the simultaneous realization of both remains a challenge. In this study, we propose a novel design of a rotary motor that can be fabricated using currently available technology, DNA origami, and validate its functionality by simulations with practical parameters. We demonstrate that the motor rotates unidirectionally and processively in the direction defined by the structural asymmetry. The motor also exhibits scalability in that increasing the number of motor legs allows for a larger speed, run length, and stall force. Because of its simple mechanism, a broad range of applications is expected.

## Statement of Significance

Biological molecular motors are the most sophisticated nanomachines in nature. Despite a long research history, we have yet to understand how they work in detail. A simple and promising approach for this purpose is to build artificial molecular motors. The process of achieving them helps us to understand how biological motors are designed. Some artificial motors have already been achieved. However, each realization implements only part of the characteristics that biological motors possess. In this work, we propose a novel motor mechanism that simultaneously implements two essential characteristics: scalability and directionality. The results would help us improve the biophysics of molecular motors and contribute to achieving high-performance artificial molecular motors with possible industrial applications.

## Introduction

Artificial molecular motors with autonomous functionality are expected to open new dimensions in biophysics[1,2]. They may serve as nano-sized chemically-fueled actuators for, for example, artificial muscle. The attempt to realize artificial molecular motors itself is also expected to improve our understanding of chemo-mechanical coupling at the nanoscale and advance biophysics. A significant trend in fabricating artificial molecular motors is to exploit DNA nanotechnologies with the help of nuclease enzymes. The enzyme cleaves fuel DNA or RNA strands for liberating free energy change required for driving the motors[1].

A molecular motor needs to implement three ingredients for the unidirectional motion: driving force, chemo-mechanical coupling, and structural asymmetry. The driving force is the free energy consumption liberated by, for example, the cleavage of fuel molecules. The motor's chemo-mechanical cycle couples free energy consumption and a unidirectional motion. Since the physics laws governing the motor motion are spatially symmetric, the translation direction is not defined without structural asymmetry. An additional ingredient necessary for practical applications is scalability, the ability for multiple units to work in parallel so that the device amplifies velocity and force. A prominent example is skeletal muscle[3], which consists of thousands of myosin II motors and realizes macroscopic contraction amounting to the length of $\sim$ cm and the force of $\sim$ N.

In general, a translational molecular motor makes a unidirectional motion by dissociating at its rear side from the

stator and binding at its front side to the stator. Biological molecular motors such as kinesin and myosin V realize such directional biasing despite the fact that their rear and front legs (or often called heads) are identical[4,5]. They exploit a conformational change of the legs to make asymmetric leg-rail interaction. On the other hand, synthetic motors created so far have exploited simpler mechanisms to achieve the forward-to-backward bias. Two primary biasing mechanisms are burnt-bridge Brownian ratchet (BBR) and bi-pedal motors.

The BBR motor irreversibly disrupts rail molecules as fuel at the rear so that the motor inevitably moves forward by blocking backward motion[6–11]. Thus, the motor creates a fuel gradient in the rail and translates by self-avoiding Brownian motion. The outstanding feature of the BBR motors is their scalability. Their simple chemo-mechanical mechanism allows one to increase the number of "legs" working in parallel to improve speed and force. However, BBR motors have an inherent limitation in directionality due to the lack of structural asymmetry; they translate in the direction determined by the first step, which is randomly chosen by fluctuations. Therefore, the ensemble-averaged speed vanishes unless the initial state is biased. Also, since they cleave the fuel molecules served as part of the stator, a rotational mechanism in which the rotor iteratively passes each location of the stator is not feasible.

The bi-pedal motors are able to walk on a track by a hand-over-hand mechanism in the direction defined by the structural asymmetry[12–14]. The motion is processive because the fuel is supplied from the solution, and the motor does not disrupt the stator. However, the scalable extension necessary for practical use is not straightforward.

This work proposes a novel motor mechanism that simultaneously inherits directionality and scalability and implements the mechanism in a rotary motor. A rotor moves autonomously and processively in a cylindrical stator in the direction defined by the structural asymmetry of the stator. The rotor's motion combines rotations around the rotor axis and orbital revolutions along the inner side of the stator. The stator implements fuel replacement, which allows processive motion of the rotr. The structure and chemo-mechanical mechanism are designed so that the motor can be fabricated by DNA origami technology[15,16]. We conducted extensive numerical simulations with practical physical parameters to validate the concept.

## Brief methods

### Motor design.

The motor consists of a rotor shaft with a square-pillar shape and a stator with a hexagonal-cylinder shape (Fig. 1). We designed the structure using caDNAno, software for designing DNA-origami structures, to ensure that the structure is fabricable by DNA nanotechnology[17]. Geometrical parameters obtained by caDNAno were used for the simulations (Table 1).

On each side of the rotor and stator, $N$ single DNA strands are lined up in a row. The motor alternatively iterates a state with connections in a single side and a state with connections in double sides(Fig. 1b). We do not consider states having connections in triple sides simultaneously time since they can be prevented by carefully designing the structures in experiments.

The strands on the rotor and stator are denoted as R and S, respectively. Steric hindrances on the stator bias the stable position of angle $\phi$ of S by electrostatic repulsion and introduce structural asymmetry.

The fuel DNA strands F dispersed in the solution serve as a linker connecting the rotor and stator. The sequence of F is designed so that each end of F hybridizes to R and S, respectively. An F-R binding is unstable, while an F-S binding is stable. Hence, most R is single-stranded, while most S is bound by F (Fig. 1b). Due to the instability of the F-R binding, a single S-F-R connection is unstable. However, multiple S-F-R connections are stabilized.

A nicking enzyme dispersed in the solution cleaves F hybridized to R. The nicking site is in the region where F and R are hybridized (Fig. 1c). Since F-R binding is unstable, the cleavage is basically limited to the F strands in the S-F-R connections. Consequently, the cleavage reactions of F depend on the rotor-stator conformation, where F strands connect the rotor and stator, while the conformation is changed by the cleavage reactions. Thus, the tuned binding stability among F, S, and R implements a chemo-mechanical coupling. The cleavage of F provides a free energy change necessary for driving a unidirectional motion. The cleaved products of F left on R and S will readily dissociate. Then, intact F dispersed in the solution will bind to S.

The mechanism will be elaborated in the results section.

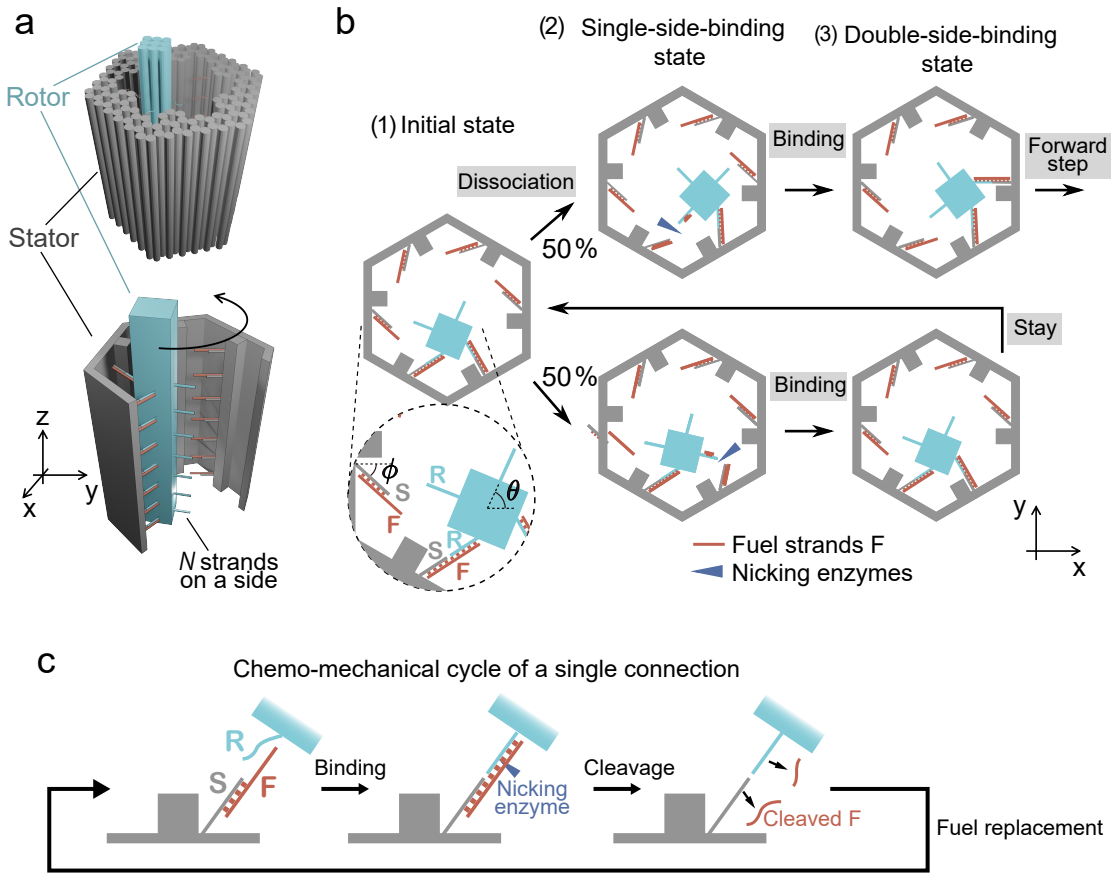


**Figure 1.** The design of the motor structure and reaction scheme. **a**, Schematic of structure design. The top shows the structure designed by caDNAno. The bottom shows the coarse-grained structure used for the simulation. A side wall of the stator is removed so that the internal structure is visible. **b**, Reaction scheme in a cross view. Although there are $N$ strands in each row, only a single set of strands is shown at each location for simplicity. **c**, Chemo-mechanical cycle of a single connection. Only a single set of S and R is shown for simplicity, although multiple sets exist.

### Simulation overview.

We developed a stochastic simulation model based on Gillespie algorithm[18]. The thermal relaxation time of the mechanical degrees of freedom, including the motor position and angles of S and R, is typically much faster than the time scale of chemical dynamics, including the hybridization, dissociation, and fuel cleavage. Therefore, we reasonably assumed that the mechanical degrees of freedom are always equilibrated and simulated the stochastic chemical transitions among the local equilibrium states corresponding to distinct chemical states by the Gillespie algorithm. The Gillespie algorithm reproduces the exact dynamics of stochastic Markovian systems with given reaction rates. The reaction rates are determined based on the free energy of each state so that the rates satisfy the local detailed balance. The parameters are determined based on the physical and chemical properties of the system. See Methods for details.

## Results

### Directionality.

We explored the conditions for the motor to translate unidirectionally, explicitly focusing on the dependence on the cleavage rate $k_{\mathrm{cut}}$. The results indicate three distinct operational modes depending on $k_{\mathrm{cut}}$; the self-directed

unidirectional motion, Brownian motion, and BBR motion (Fig. 2a–d).

### *Self-directed unidirectional motion.*

We observed a unidirectional motion by tuning $k_{\mathrm{cut}}$ to intermediate values significantly less than the binding rate of F to R and S, $k_{\mathrm{on}} = 1\,\mathrm{s}^{-1}$ (Fig. 2a, c). Such unidirectional motion was not observed without the structural asymmetry (Fig. 2c, e) nor fuel consumption with vanishing $k_{\mathrm{cut}}$ (Fig. 2a). The direction was inverted with opposite structural asymmetry (Fig. 2c). These results validate that the motor is driven by the free energy consumption in the direction defined by the structural asymmetry. Note that the motor revolves in the stator while rotating on its own axis.

The unidirectional motion suggests a biasing mechanism that favors the dissociation of the rear side in the two-side-binding state, binding at the front side in the one-side-binding state, or both. These possibilities will be examined in the following.

Under the present condition with intermediate $k_{\mathrm{cut}}$, the connections by F are mainly broken by the enzymatic cleavage rather than by the denaturation. The fuel cleavage rates at the front and rear sides are the same in the two-side-binding state. Since $k_{\mathrm{on}} > k_{\mathrm{cut}}$, the cleavage of all the connections on the side takes a long time, sufficient for each connection to repeat multiple cycles of fuel binding, cleavage, and replacement before the dissociation. Therefore, the number of connections at each side fluctuates in a random-walk manner. As a result, the bindings of the front and rear sides stochastically dissociate at similar rates. That is, there is no forward-to-backward bias in the dissociation process.

On the other hand, in a one-side-binding state, the steric hindrance tilts the motor forward and makes the forward binding more feasible than the backward binding. The speed increased with $|\phi_{\mathrm{eq}}|$ as far as $|\phi_{\mathrm{eq}}| \leq 45°$ by enhancing the binding bias. With $|\phi_{\mathrm{eq}}| > 45°$, the binding of the rotor and the stator becomes unstable, resulting in the fast dissociation of the motor (data not shown).

Thus, only the binding is biased to the forward direction. Hence, on average, the motor makes a forward step per roughly two chemo-mechanical cycles. All the connections on the side may dissociate even in the one-side-binding state, which results in the decomposition of the motor-stator complex.

The speed increased with $k_{\mathrm{cut}}$ (Fig. 2a) since the dissociation is the rate-limiting step. The average run length, evaluated as the average traveling distance until both sides dissociate from the stator, decreased with $k_{\mathrm{cut}}$ due to the increase in the dissociation rate at the one-side-binding state (Fig. 2f). This indicates the trade-off between speed and processivity.

### *Brownian motion.*

At negligible $k_{\mathrm{cut}}$, the motor exhibited a Brownian motion with vanished mean speed (Fig. 2a, b). Since driving force is absent at vanishing $k_{\mathrm{cut}}$, a unidirectional motion is forbidden by the microscopic reversibility[19]. Although the forward binding is still more favorable than the backward binding because of the structural asymmetry, the dissociation has the same bias. It cancels out the binding bias.

### *BBR motion.*

When we increased $k_{\mathrm{cut}}$ to the values comparable to the fuel binding rate $k_{\mathrm{on}} = 1\,\mathrm{s}^{-1}$, a unidirectional motion was still observed (Fig. 2d). With such large $k_{\mathrm{cut}}$, the fuel cleavage proceeds faster than the fuel replacement, keeping the fraction of S possessing F small. At a single-side-binding state, the backward step is prevented due to the lack of available intact F strands on S; the binding is biased to the forward direction, resulting in unidirectional motion.

However, the rotational direction was random and different from run to run, manifested in the symmetric two-peak frequency distribution (Fig. 2a). The ensemble-average speed vanished despite the structural asymmetry, and the variance was significant (Fig. 2a). Furthermore, the rotation was not processive; the motor readily dissociated from the stator after a few revolutions (Fig. 2d, f). In the case of the rotary motor, the fuel must be replaced immediately. Otherwise, the rotor will soon dissociate from the stator after a single revolution. These are the distinct characteristics of a BBR-type mechanism.

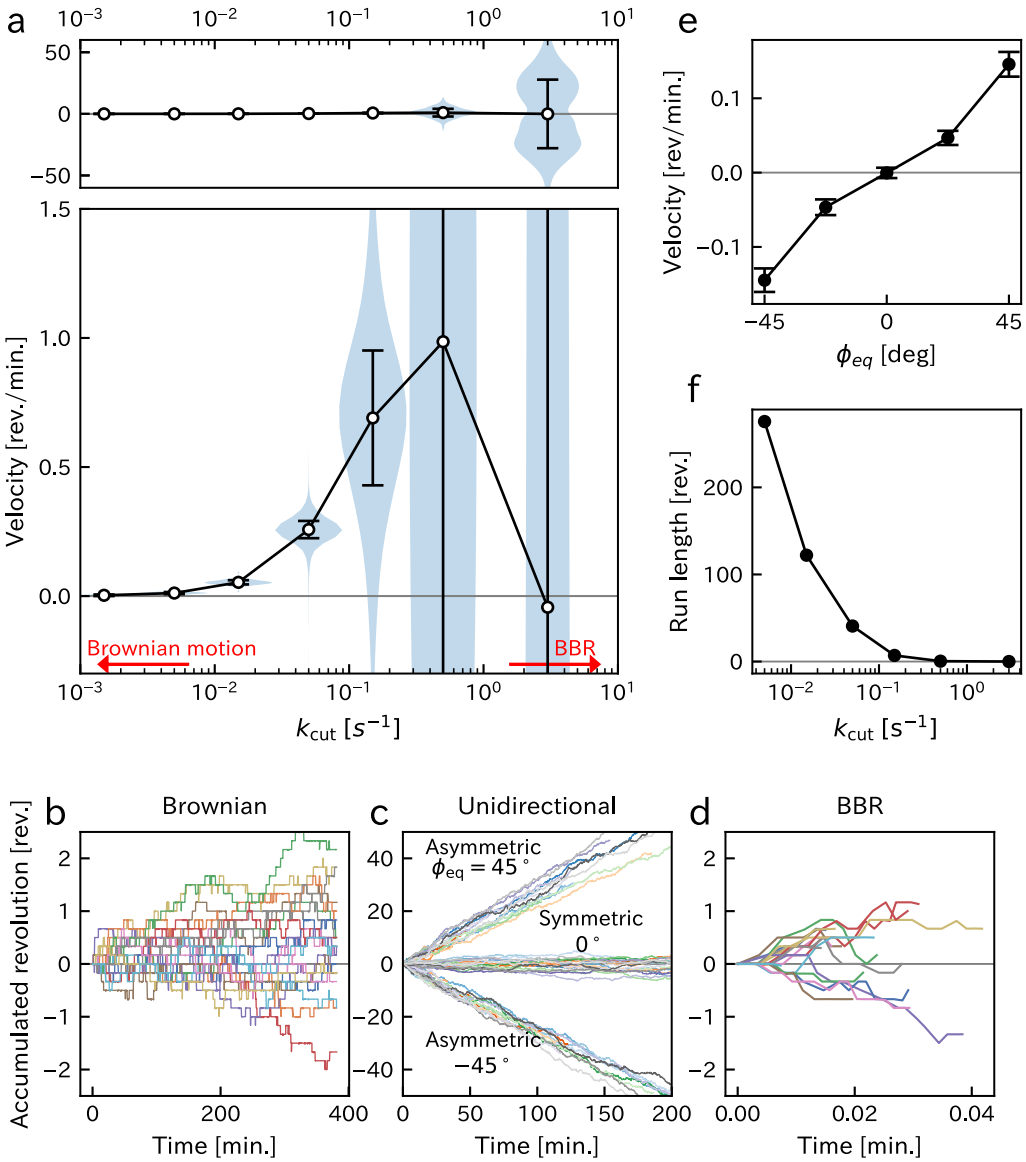


**Figure 2.** Conditions for unidirectional motion. **a**, Mean velocity with the violin plot indicating the frequency by width. The bottom panel shows the magnification. The numbers of runs are 4986, 999, 999, 908, 70, 70, 70, respectively, from right to left. **b**, Simulated trajectories of the revolutions (20 runs in each group) with $k_{\mathrm{cut}} = 0.05\,\mathrm{s}^{-1}$ and $\phi_{\mathrm{eq}} = 45°$ (top), 0° (middle), and −45° (bottom). Different colors correspond to independent simulations. **c**, Average velocity vs $\phi_{\mathrm{eq}}$. $k_{\mathrm{cut}} = 0.05\,\mathrm{s}^{-1}$. **d**, Trajectories with $k_{\mathrm{cut}} = 5 \times 10^{-5}\,\mathrm{s}^{-1}$.**e**, Trajectories with $k_{\mathrm{cut}} = 1.5\,\mathrm{s}^{-1}$. The number of runs is 50 for each point. **f**, Run length vs $k_{\mathrm{cut}}$. $N = 6$. $\phi_{\mathrm{eq}} = 45°$ except for **c**. Error bars in **a** and **e** represent standard deviations.

**Scalability.**

We evaluated the scalability of the unidirectional motion ($k_{\mathrm{cut}} = 005s^{-1}$) in terms of the $N$ dependence of the velocity, run time, and run length. The run time and run length quantify the motor processivity and are defined as the time duration and the traveling distance, respectively, before both sides dissociate from the stator.

We found that the speed decreased with $N$ (Fig. 3a), while the run time and length increased with $N$ (Fig. 3b, c). As we have seen, the speed increases with $k_{\mathrm{cut}}$ (Fig. 2a). However, the motor rapidly dissociates at large $k_{\mathrm{cut}}$, decreasing the run length (Fig. 2f). This trade-off between the speed and run length (Fig. 3e) practically limits the maximum speed. Nonetheless, by increasing $N$, we can suppress the dissociation and raise the threshold for $k_{\mathrm{cut}}$ to increase the velocity further. Thus, the motor inherits scalability that the increase in $N$ allows larger velocity and run length.

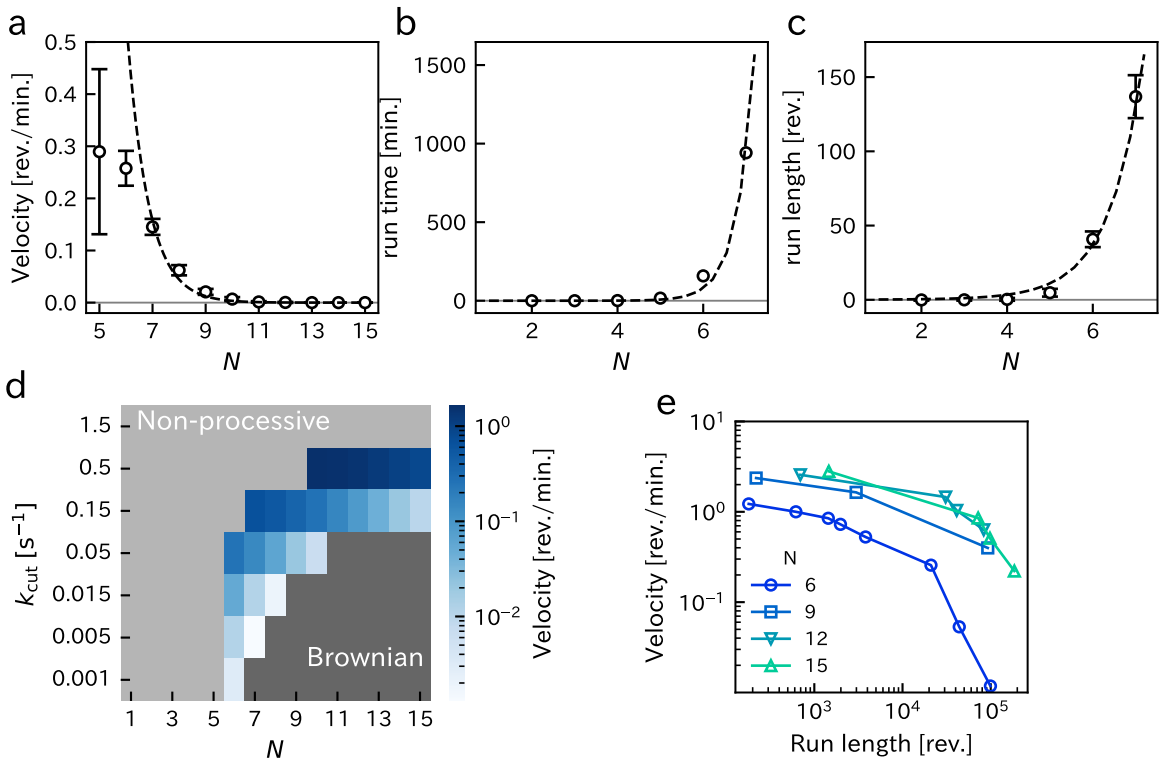


**Figure 3.** Dependence of velocity and run length on $N$. **a**, Velocities. Velocities for $N = 4$ or less are not shown because the errors were too large. **b**, Run time. The dissociation is too fast with $N = 1$, and dissociation did not occurs with $N \geq 8$. **c**, Run length. The dashed lines in **a** – **c** are obtained by the global fitting of $aN(1+\kappa)^{-N}$, $b/N^2/(1+\kappa)^{-2N}$, and $c/N/(1+\kappa)^{-N}$, respectively, with $a = 402$, $b = 0.00015$, $c = 0.050$, and $\kappa = 3.1$ (see Eq. 2). **d** Velocities as the function of $k_{\mathrm{cut}}$ and $N$. The light gray region corresponds to a non-processive motion (the run length is less than ten revolutions). The dark gray region corresponds to Brownian motion without unidirectional motion. **e**, Velocities vs run length. Points in the same curve have different $k_{\mathrm{cut}}$ values. Error bars in **a** – **c** indicate the standard deviations. $k_{\mathrm{cut}} = 0.05\,\mathrm{s}^{-1}$ for **a** – **c**. The number of runs is 70 for each point.

The rate-limiting of the chemo-mechanical cycle is the dissociation of a side that requires the cleavages of all connections in the side. Therefore, it is reasonable that the increase in $N$ slows down the motor while enhancing the processivity. We derive the explicit $N$ dependence of the velocity, run time, and run length based on a simple estimation of the dissociation rate of a single side. For simplicity, the binding dynamics of each connection are assumed to be equilibrated. Let $p$ be the probability that a pair of R and S on a side are connected by F. Let $k_+$ and $k_-$ be the binding and dissociation rates of a single connection, respectively. We obtain $p = k_+/(k_+ + k_-) = K/(1+K)$ by solving the detailed balance $pk_- = (1-p)k_+$, where $K \equiv k_+/k_-$. The probability that there are $n$ ($0 \leq n \leq N$)

connections in the side obeys the binomial distribution

$$P_n = \begin{pmatrix} N \\ n \end{pmatrix} p^n (1-p)^{N-n} = \begin{pmatrix} N \\ n \end{pmatrix} \frac{K^n}{(1+K)^N}. \tag{1}$$

The dissociation rate of a side is calculated as

$$D_N = \frac{P_1}{1-P_0} k_- = \frac{k_+ N}{(1+K)^N - 1} \quad \sim k_+ N (1+K)^{-N} \quad (N \gg 1). \tag{2}$$

Here, $1-P_0$ is a normalization factor and corresponds to the probability that the side is bound.

A coarse scaling discussion implies that the velocity is proportional to $D_N$, since the side dissociation is the rate-limiting step under the present condition. This may explain the exponential decrease of the velocity with $N$ for large $N$ (Fig. 3a). On the other hand, the run time scales as $D_N^{-2}$, since both sides need to dissociate. The run length is calculated as the steady velocity times the run time and scales as $D_N/D_N^2 = D_N^{-1}$. We successfully fitted the velocity, run length and run time by these scaling relations at large $N$ (Fig. 3a–c).

### Stall force.

Next, we evaluated the stall force of the unidirectional motion (Fig. 4a, b). The stall force is the magnitude of hindering external force necessary for stalling the motor motion and quantifies the maximum force the motor can exert. As noted, the motor motion combines rotations around the rotor axis and orbital revolutions along the inner side of the stator. Hence, we evaluate the stall force rather than stall torque.

We induced an external hindering force to the rotor in the direction perpendicular to the rotor revolution. As the magnitude of the applied force increased, the velocity decreased, vanished, and reversed (Fig. 4a). The stall force, evaluated as the external force where the speed vanished, increased with $N$ (Fig. 4b). Note that the motor's unidirectional motion originates from the leg's tilt due to the steric hindrance (Fig. 2e). Therefore, reducing the tilt caused by external hindering force is expected to slow down the motor. Since the hindering force is distributed over the connections, the increase in $N$ suppresses the tilt reduction and increases the stall force.

We obtained a stall force larger than 10 pN (Fig. 4b), which is larger than the stall force of artificial bi-pedal DNA motor[13], kinesin (5–7pN)[20], and myosin V (2–3pN)[21]. The stall torque is roughly estimated to be $\sim 100$ pNnm using 10 nm as the rotational radius. This value exceeds the stall torque of $F_1$-ATPase ($\sim 40$ pNnm)[22]. The stall torque of the bacterial flagellar motor ($\sim 1000$ pNnm)[23] is much larger because it is strongly driven by proton motive force. A large stall force of $\sim 150$ pN was reported for a BBR-type motor having more than a thousand connections[24]. However, such a BBR motor does not realize self-directed unidirectional motion.

### Fuel efficiency.

Finally, we evaluated the efficiency of the unidirectional motion in terms of fuel consumption. We define the fuel efficiency $\eta_0$ as the mean number of net forward steps divided by the mean number of consumed fuel molecules during a certain time period. Since a motor with larger $N$ consume more fuel molecules, we define a net fuel efficiency $\eta = N\eta_0$ (Fig. 4c). Note that $\eta$ can be generally larger than one by definition.

We found that $\eta < 0.5$ and that $\eta$ decreases with $N$. If all the fuel cleavages contribute to the kinetics, $\eta$ amounts to the maximum value of 0.5 since the motor steps every two cycles on average. The decrease of $\eta$ with $N$ may be explained as follows. The cleaved fuels may be replaced by intact fuel strands before all the connections in the side are cleaved. Such "resurrection" of the fuel wastes fuel consumption, and the efficiency decreases. As $N$ increases, the time for all the connections in a side to be cleaved increases; therefore, the futile fuel consumption increases. Previous studies on BBR motors also reported decreased efficiency with the number of connections[25].

## Discussion

This study proposed a novel design of an artificial molecular motor with controlled directionality and scalability. The motor implements fuel replacements, unlike BBR motors, enabling rotational motions. The structure is designed

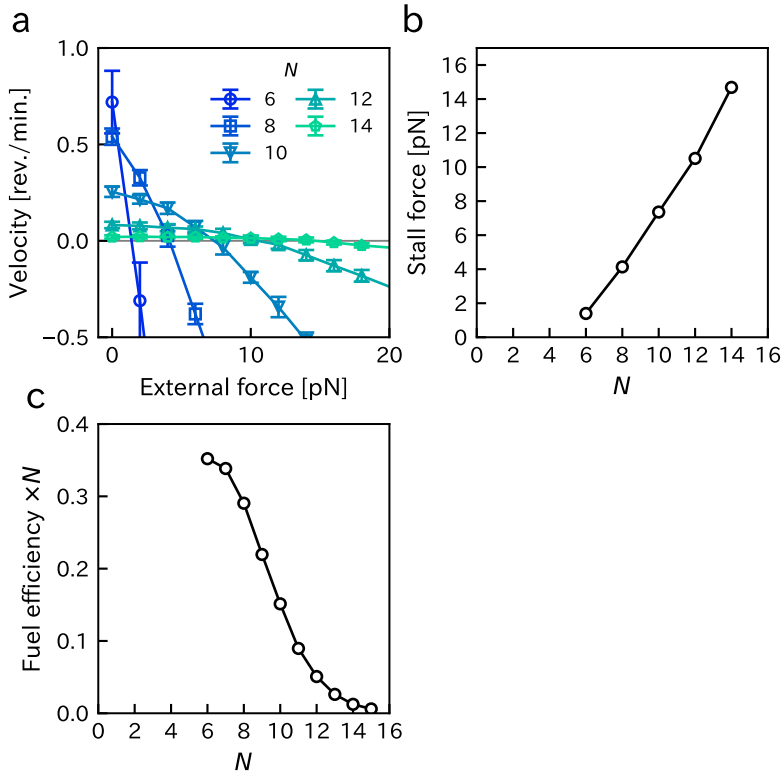


**Figure 4.** Stall force and fuel efficiency. $k_{\mathrm{cut}} = 0.15\,\mathrm{s}^{-1}$. **a**, Velocity under different magnitudes of external force. The stall force is evaluated as the force where the velocity vanishes. Error bar indicates the standard deviation. **b**, Magnitudes of stall force for various $N$. **c**, Net fuel efficiency $\eta$. The number of runs is 20 for each point.

so that it is fabricable by currently available technology. The motor exhibited a processive unidirectional motion in the direction defined by the structural asymmetry. The simplicity of the mechanism makes the motor scalable. Increasing the maximum number of connections $N$ allows larger velocity, run length, and stall force (Fig. 3a-c). Thus, the design has the advantages of both the track-walking bi-pedal motors and multivalent BBR motors.

However, the velocity was limited to a relatively small value of $\sim 1$ rev./min. (Fig. 4a). The net fuel efficiency $\eta$ was also limited to a value less than 0.5 (Fig. 4c). This fact highlights the sophisticated chemo-mechanical coupling mechanisms of biological molecular motors. To enhance motor performance, it is critical to bias also the dissociation process so that the rear side dissociates more readily than the front side. Since the front and rear sides are identical, we need an additional mechanism to implement such bias. Biological molecular motors such as kinesin and myosin V utilize conformational change to achieve a significant biasing for both the binding and dissociation[4,5]. An artificial bi-pedal motor achieved the bias by using the asymmetric response of the double-helix denaturing to the direction of the mechanical load[12,26]. However, it is not straightforward to implement the scalability and these mechanisms simultaneously. A simple solution is to discriminate the accessibility of the enzyme to the front and rear sides. It has been established to precisely fix proteins on the targeted location of DNA origami structure[27]. It may be possible to cleave the connections on the rear side favorably by carefully placing the enzyme on the stator since the S-F-R connections on the front and rear sides have different equilibrium angular positions (Fig. 1b).

Experimental validation of the design is a future challenge. Rotary structures have already been fabricated with DNA origami, although autonomous functionality has not been implemented[28,29]. One of the benefits of the rotary mechanism is that precision observation is more accessible than the linear mechanism since sub-micron probes attached to the rotor can magnify the rotational motion. Note that probes do not amplify the linear motion. Issues to be solved may include the accessibility of the fuel DNA strand and enzyme into the stator cylinder and the efficient

emission of the cleaved products from the cylinder. The mechanism proposed in this study is not limited to rotary motors. Applications to other geometries, such as linear motors, are straightforward. An intriguing development includes accumulating of many motors for building a macroscopic actuator like a skeletal muscle.

## Methods

The Gillespie algorithm[18] simulates stochastic transitions among discrete states and gives exact sampling. In the following, we define the states, then the potentials and reaction rates necessary for defining the transition rates among the states.

### States.

The chemical states are defined based on the combinations of the binding states of all R and S. Each R (S) is in one of the five possible states; single-stranded, bound to free F, bound to the shorter cleaved product of F, connected to S (R) via F, or connected to a connection to S (R) via the longer cleaved product of F.

### Motor coordinates.

We assumed that the rotor motion is limited in the lateral space and does not move in the z-axis direction (Fig. 1). Thus, the rotor geometry is specified by the rotor centroid $(x, y)$ and rotational angle $\theta$.

### Potential energy.

We assumed that the mechanical dynamics of $(x, y, \theta)$ and $\theta$ are much faster than the chemical reaction dynamics and always equilibrated in each chemical state. Therefore, we use the equilibrium distribution of $(x, y, \theta)$ given by the Boltzmann distribution with a potential including the rotor-stator electrostatic repulsion, elastic extension of the double-stranded DNA, and steric hindrance for S.

DNA nanostructures are usually built in the presence of cations to suppress the electrostatic repulsion among negatively-charged DNA strands. In the simulation, we used the Debye length of $\lambda_{\mathrm{D}} = 1.25\,\mathrm{nm}$ assuming the presence of 20 mM $MgCl_2$. Although a base pair contains two charged phosphate groups, we assumed that only a single side of the phosphate group exposed at the surfaces of DNA origami is involved in electrostatic repulsion because $\lambda_{\mathrm{D}}$ is smaller than the diameter of the double-stranded DNA. Furthermore, we assumed that interaction among phosphate groups at the rotor and stator surfaces is limited to those within a distance smaller than $\lambda_{\mathrm{D}}$ and the interaction between only the nearest double strands is effective due to the Debye shielding. When two double-stranded DNA are adjacent, a phosphate group of either strand has at most 7.5 phosphate groups in the other strand within $\lambda_{\mathrm{D}}$. Thus, the electrostatic potential between the rotor at $x$, $y$, and $\theta$ and the stator leads to

$$G_{\mathrm{ele}}(x, y, \theta) = \frac{7.5 N_{\mathrm{p}} e^2}{4\pi\varepsilon\varepsilon_0 \lambda(x, y, \theta)} \exp\left(-\lambda(x, y, \theta)/\lambda_{\mathrm{D}}\right), \tag{3}$$

where $\lambda(x, y, \theta)$ is the shortest distance between the rotor and stator cylinder under the approximation that the rotor and stator have cylindrical shapes. $e$ is the elementary charge, $\varepsilon_0$ is the permittivity of vacuum, and $\varepsilon$ is the relative permittivity of water. $N_{\mathrm{p}} = 210$ is the number of phosphate groups in a row obtained by dividing the rotor or stator height (70 nm) by the length of a single base pair (0.33 nm).

We calculated the elastic energy of each S-F-R connection as a linear spring with the spring constant of $k = ES/L_{\mathrm{eq}}$. Here, $E$ is Young's modulus $E$, $S$ is the cross-sectional area $S$, and $L_{\mathrm{eq}} = 8\,\mathrm{nm}$ is the equilibrium length of the double-stranded connection S-F-R. Thus, the total elastic energy is calculated as

$$G_{\mathrm{elast}}(x, y, \theta) = \sum_i \frac{c_i}{2} k [L_i(x, y, \theta) - L_{\mathrm{eq}}]^2, \tag{4}$$

where $L_i$ is the length of the $i$-th connection. $c_i = 1$ if $i$-th S and R are connected by F and 0 otherwise.

The electrostatic repulsion by the steric hindrances is modeled by a harmonic potential. Let $\phi_i$ be the angle of the $i$-th S strand with the normal direction of the cylinder's inner surface as the origin. We calculated the potential as

$$G_{\mathrm{hind}}(x,y,\theta) = \sum_i \frac{1}{2} k_\theta [\phi_i(x,y,\theta) - \phi_{\mathrm{eq}}]^2, \tag{5}$$

where $G_{\mathrm{hind}}$ is the harmonic potential for the stator-side angle of the S-F-R connections, $k_\theta = 64/k_{\mathrm{B}}T$ is the angular spring constant. Here, $k_{\mathrm{B}}$ is the Boltzmann constant, and $T$ is the absolute temperature, and $\phi_{\mathrm{eq}} = 45^\circ$ except for Fig. 2e is the equilibrium angle. The stiffness was determined so that the potential of each S is $2k_{\mathrm{B}}T$ at $\phi_i = \phi_{\mathrm{eq}} \pm 45^\circ$.

The equilibrium distribution $P(x,y,\theta)$ is given by the Boltzmann distribution

$$P(x,y,\theta) = \frac{\exp\left(-G_{\mathrm{mech}}(x,y,\theta)/k_{\mathrm{B}}T\right)}{\iiint \mathrm{d}x\mathrm{d}y\mathrm{d}\theta \exp\left(-G_{\mathrm{mech}}(x,y,\theta)/k_{\mathrm{B}}T\right)}, \tag{6}$$

where $G_{\mathrm{mech}} = G_{\mathrm{ele}} + G_{\mathrm{elast}} + G_{\mathrm{hind}}$ is the interaction potential between the rotor and stator. The trajectories in Fig. 2b–d are the expected values obtained based on $P(x,y,\theta)$.

### Reaction rates.

The reactions we consider include the binding and dissociation of DNA strands and the fuel cleavage by the enzyme. The time scale of all the dynamics is scaled with $1/k^0_{\mathrm{bind}}$, where $k^0_{\mathrm{bind}}$ is the binding rate of a free F strand to a tethered DNA strand within the volume of $(10\,\mathrm{nm})^3$. That is, $1/k^0_{\mathrm{bind}}$ defines the unit time. We estimated $k^0_{\mathrm{bind}}$ to be $500\,\mathrm{s}^{-1}$ based on a previous experiment[30].

We assume that the binding between the tethered strands, R and F-S or F-R and S, occurs only when they are within a cut-off distance $r_{\mathrm{cutoff}} = 12\,\mathrm{nm}$ defined as $1.5L_{\mathrm{eq}}$. We define a binding rate $k_{\mathrm{bind}}(x,y,\theta)$ as $k^0_{\mathrm{bind}}$ if $r_{ij}(x,y,\theta) \le r_{\mathrm{cutoff}}$ and 0 otherwise. Here, $r_{ij}$ is the distance between the $i$-th R and the $j$-th S.

For the Gillespie algorithm, we used the expected value $\langle k_{\mathrm{bind}} \rangle = \iiint \mathrm{d}x\mathrm{d}y\mathrm{d}\theta P(x,y,\theta) k_{\mathrm{bind}}(x,y,\theta)$. The dissociation rate is obtained based on the local detailed balance condition. The free energy change associated with the binding events is the mechanical free-energy change $G_{\mathrm{mech}}$ and chemical free-energy change $G_{\mathrm{chem}}$. $G_{\mathrm{chem}}$ is the summation of the free energy change by the hybridization; $-k_{\mathrm{B}}T$ for S and F or cleaved product of F, $2k_{\mathrm{B}}T$ for R and F, $6k_{\mathrm{B}}T$ for R and cleaved product of F, which are roughly determined by the typical DNA-binding parameters for the present fuel concentration. The local detailed balance condition gives $k_{\mathrm{dis}}(x,y,\theta) = k_{\mathrm{bind}}(x,y,\theta) \exp\left[(G_{\mathrm{mech}} + G_{\mathrm{chem}})/k_{\mathrm{B}}T\right]$. We used the expected value $\langle k_{\mathrm{dis}} \rangle$ for the Gillespie algorithm.

The binding rate $k_{\mathrm{on}}$ of free F in the solution to R or S was determined based on $k^0_{\mathrm{bind}}$. We assume that the binding of a free F strand in the volume of $(10\,\mathrm{nm})^3$, which corresponds to the concentration of 1.5 mM, is equal to $k^0_{\mathrm{bind}}$. This volume roughly approximates the volume within the cut-off distance $r_{\mathrm{cutoff}} = 12\,\mathrm{nm}$ subtracted by the excluded volume due to the rotor and stator structures. We let the concentration of F in the solution to be $3\,\mu\mathrm{M}$ and obtain $k_{\mathrm{on}} = k^0_{\mathrm{bind}} \cdot 3\,\mu\mathrm{M}/1.5\,\mathrm{mM} = 1\,\mathrm{s}^{-1}$. We ignored the rebinding of cleaved products of F to R and S because their concentrations are negligible compared with F. The hybridization is diffusion-limited in the present dilute condition, and the $k_{\mathrm{on}}$ does not significantly depend on the sequence[31]. Therefore, $k_{\mathrm{on}}$ is assumed to be the same for all the sequences. The local detailed balance condition gives sequence-dependent dissociation rate $k_{\mathrm{off}} = k_{\mathrm{on}} \exp\left(G_{\mathrm{chem}}/k_{\mathrm{B}}T\right)$.

## Acknowledgements

This work was supported by KAKENHI (18H05427, 19H01857, and 23H01136).

## Author contributions

K.I. conducted the simulations and analyzed the results, K.I., Y.S., S. T. designed the research and wrote the manuscript. All authors reviewed the manuscript.

**Table 1.** Geometrical and reaction parameters.

| Description | Label | Value | Unit |
|---|---|---|---|
| Inner diameter of stator | - | 31 | nm |
| Outer diameter of rotor | - | 7.5 | nm |
| Height of stator and rotor | - | 70 | nm |
| Number of S and R strands in a row | $N$ | $1 \sim 15$ | |
| Equilibrium length of S-F-R connection | $L_{\mathrm{eq}}$ | 8 | nm |
| Spring constant of S-F-R connection | $k$ | 24.7 | $k_{\mathrm{B}}T/\mathrm{nm}^2$ |
| Equilibrium angle of S | $\phi_{\mathrm{eq}}$ | 45 | degree |
| Angular spring constant of S (angular) | $k_\theta$ | $64/\pi^2$ | $k_{\mathrm{B}}T$ |
| Debye length | $\lambda_{\mathrm{D}}$ | 1.25 | nm |
| Cut-off length | $r_{\mathrm{cutoff}}$ | 12 | nm |
| $\Delta G$ of S-F hybridization in solution | - | -1 | $k_{\mathrm{B}}T$ |
| $\Delta G$ of R-F hybridization in solution | - | 2 | $k_{\mathrm{B}}T$ |
| $\Delta G$ of R-decomposed product hybridization | - | 6 | $k_{\mathrm{B}}T$ |
| Concentration of F | - | 3 | μM |
| Binding rate of two tethered strands within $r_{\mathrm{cutoff}}$ | $k^0_{\mathrm{bind}}$ | 500 | $\mathrm{s}^{-1}$ |
| Binding rate of free F in solution to R and S | $k_{\mathrm{on}}$ | 1 | $\mathrm{s}^{-1}$ |
| Enzymatic cleavage rate | $k_{\mathrm{cut}}$ | 0.0015–1.5 | $\mathrm{s}^{-1}$ |

## Additional information

The authors declare no conflict of interest.

## References


1. Wang, Z., Hou, R. & Loh, I. Y. Track-walking molecular motors: a new generation beyond bridge-burning designs. *Nanoscale* **11**, 9240–9263, DOI: 10.1039/C9NR00033J (2019).
2. Kassem, S. *et al.* Artificial molecular motors. *Chem. Soc. Rev.* **46**, 2592–2621, DOI: 10.1039/c7cs00245a (2017).
3. Alberts, B., Heald, R., Johnson, A. D., Morgan, D. & Raff, M. *Molecular Biology of the Cell* (Garland, 2022), 7th edn.
4. Yildiz, A., Tomishige, M., Vale, R. D. & Selvin, P. R. Kinesin walks hand-over-hand. *Science* **303**, 676–678, DOI: 10.1126/science.1093753 (2004).
5. Yildiz, A. *et al.* Myosin V walks hand-over-hand: Single fluorophore imaging with 1.5-nm localization. *Science* **300**, 2061–2065, DOI: 10.1126/science.1084398 (2003).
6. Bath, J., Green, S. J. & Turberfield, A. J. A free-running DNA motor powered by a nicking enzyme. *Angew. Chem. Int. Ed.* **44**, 4358–4361, DOI: 10.1002/anie.200501262 (2005).
7. Lund, K. *et al.* Molecular robots guided by prescriptive landscapes. *Nature* **465**, 206–210, DOI: 10.1038/nature09012 (2010).
8. Wickham, S. F. J. *et al.* Direct observation of stepwise movement of a synthetic molecular transporter. *Nat. Nanotech.* **6**, 166–169, DOI: 10.1038/nnano.2010.284 (2011).
9. Yehl, K. *et al.* High-speed DNA-based rolling motors powered by RNase H. *Nat. Nanotech.* **11**, 184–190, DOI: 10.1038/nnano.2015.259 (2016).
10. Bazrafshan, A. *et al.* Tunable DNA origami motors translocate ballistically over $\mu$m distances at nm/s speeds. *Angew. Chem.* **132**, 9601–9608, DOI: 10.1002/ange.201916281 (2020).

**11.** Bazrafshan, A. *et al.* DNA gold nanoparticle motors demonstrate processive motion with bursts of speed up to 50 nm per second. *ACS Nano* **15**, 8427–8438, DOI: 10.1021/acsnano.0c10658 (2021).

**12.** Liu, M. *et al.* Biomimetic autonomous enzymatic nanowalker of high fuel efficiency. *ACS Nano* **10**, 5882–5890, DOI: 10.1021/acsnano.6b01035 (2016).

**13.** Hu, X., Zhao, X., Loh, I. Y., Yan, J. & Wang, Z. Single-molecule mechanical study of an autonomous artificial translational molecular motor beyond bridge-burning design. *Nanoscale* **13**, 13195–13207, DOI: 10.1039/d1nr02296b (2021).

**14.** Bath, J., Green, S. J., Allen, K. E. & Turberfield, A. J. Mechanism for a directional, processive, and reversible DNA motor. *Small* **5**, 1513–1516, DOI: 10.1002/smll.200900078 (2009).

**15.** Rothemund, P. W. Folding DNA to create nanoscale shapes and patterns. *Nature* **440**, 297–302, DOI: 10.1038/nature04586 (2006).

**16.** Bath, J. & Turberfield, A. J. DNA nanomachines. *Nat. Nanotech.* **2**, 275–284, DOI: 10.1038/nnano.2007.104 (2007).

**17.** Douglas, S. M. *et al.* Rapid prototyping of 3D DNA-origami shapes with caDNAno. *Nuc. Acids Res.* **37**, 5001–5006, DOI: 10.1093/nar/gkp436 (2009).

**18.** Gillespie, D. T. Exact stochastic simulation of coupled chemical reactions. *J. Phys. Chem.* **81**, 2340–2361, DOI: 10.1021/j100540a008 (1977).

**19.** Astumian, R. D. Microscopic reversibility as the organizing principle of molecular machines. *Nat. Nanotechnol.* **7**, 684–688, DOI: 10.1038/nnano.2012.188 (2012).

**20.** Svoboda, K. & Block, S. M. Force and velocity measured for single kinesin molecules. *Cell* **77**, 773–784, DOI: 10.1016/0092-8674(94)90060-4 (1994).

**21.** Mehta, A. D. *et al.* Myosin-V is a processive actin-based motor. *Nature* **400**, 590–593, DOI: 10.1038/23072 (1999).

**22.** Toyabe, S., Watanabe-Nakayama, T., Okamoto, T., Kudo, S. & Muneyuki, E. Thermodynamic efficiency and mechanochemical coupling of $F_1$-ATPase. *Proc. Nat. Acad. Sci.* **108**, 17951–17956, DOI: 10.1073/pnas.1106787108 (2011).

**23.** Sato, K., Nakamura, S., Kudo, S. & Toyabe, S. Evaluation of the duty ratio of the bacterial flagellar motor by dynamic load control. *Biophys. J.* **116**, 1952–1959, DOI: 10.1016/j.bpj.2019.04.004 (2019).

**24.** Blanchard, A. T. *et al.* Highly polyvalent DNA motors generate 100 pN of force via autochemophoresis. *Nano Lett.* **19**, 6977–6986, DOI: 10.1021/acs.nanolett.9b02311 (2019).

**25.** Leighton, M. P. & Sivak, D. A. Performance scaling and trade-offs for collective motor-driven transport. *New J. Phys.* **24**, 013009, DOI: 10.1088/1367-2630/ac3db7 (2022).

**26.** Tee, S. R., Hu, X., Loh, I. Y. & Wang, Z. Mechanosensing potentials gate fuel consumption in a bipedal DNA nanowalker. *Phys. Rev. Appl.* **9**, DOI: 10.1103/physrevapplied.9.034025 (2018).

**27.** Kong, G. *et al.* DNA origami-based protein networks: from basic construction to emerging applications. *Chem. Soc. Rev.* **50**, 1846–1873, DOI: 10.1039/d0cs00255k (2021).

**28.** Ketterer, P., Willner, E. M. & Dietz, H. Nanoscale rotary apparatus formed from tight-fitting 3D DNA components. *Sci. Adv.* **2**, DOI: 10.1126/sciadv.1501209 (2016).

**29.** Pumm, A.-K. *et al.* A DNA origami rotary ratchet motor. *Nature* **607**, 492–498, DOI: 10.1038/s41586-022-04910-y (2022).

**30.** Kumar, S., Weisburd, J. M. & Lakin, M. R. Structure sampling for computational estimation of localized DNA interaction rates. *Sci. Rep.* **11**, DOI: 10.1038/s41598-021-92145-8 (2021).

**31.** Tawa, K., Yao, D. & Knoll, W. Matching base-pair number dependence of the kinetics of DNA-DNA hybridization studied by surface plasmon fluorescence spectroscopy. *Biosens. Bioelect.* **21**, 322–329, DOI: 10.1016/j.bios.2004.10.024 (2005).